

---

# COLLECTIVE ACTION AND ENTANGLEMENT OF MAGNETICALLY ACTIVE LIQUID CRYSTAL ELASTOMER RIBBONS

---

A PREPRINT

A. DANA, C. BENSON, M. SIVAPERUMAN KALAIRAJ, K.HELLIKSON, S.M. GEORGE, D.C. CHIMENE, J.A. GIBSON, S. TASMIN, P.A. KOHL, Y. LI, M.K. ABDELRAHMAN, V.P. PATIL, T.H. WARE\*

<https://orcid.org/0000-0001-8515-4575> Asaf Dana

<https://orcid.org/0000-0001-7996-7393> Taylor H. Ware\*

Department of Materials Science and Engineering, Texas A&M University, College Station, TX 77843, USA

Department of Biomedical Engineering, Texas A&M University, College Station, TX 77843, USA

**Christian Benson, Manivannan Sivaperuman Kalairaj, Kayla Hellikson,**

**Jared A. Gibson, Seelay Tasmim, David C. Chimene**

Department of Biomedical Engineering, Texas A&M University, College Station, TX 77843, USA

**Sasha M. George, Mustafa K. Abdelrahman**

Department of Materials Science and Engineering, Texas A&M University, College Station, TX 77843, USA

**Phillip A. Kohl, Youli Li**

Materials Research Laboratory, University of California - Santa Barbara, Santa Barbara, CA 93106, USA

**Vishal P. Patil**

Department of Mathematics, University of California, San Diego, La Jolla, CA 92093, USA

## ABSTRACT

Interactions between active individuals in animal collectives lead to emergent responses that remain elusive in synthetic soft matter. Here, shape-morphing polymers are used to create bio-inspired transient solids that self-assemble with controlled mechanical properties and disassemble on demand. Dilute-suspensions of magnetic, heat-responsive liquid crystal elastomer ribbons mechanically interlock, inducing reversible aggregation. A mathematical model is developed that sheds light on the role of topological mechanisms in aggregation. Aggregation was favored for ribbons with moderate curvature at 25°C above crosslinking temperature as compared to flat ribbons or higher curvature ribbons at higher temperatures. The ribbon suspensions reversibly transition between fluid- and solid-like states, exhibiting up to 6 orders-of-magnitude increase in the storage moduli of the entangled aggregates compared with the liquid dispersions. Controlled dissociation is induced by imparting kinetic energy to the individual ribbons at high magnetic field rotation speeds (> 200 RPM). Ribbon shape and the medium in which dissociation occurs were shown to govern disassembly. Imparting dynamic collective behaviors into synthetic systems may enable a range of potential applications from bio-inspired soft robotics to injectable biomaterials.

**Keywords** liquid crystal elastomers · collective action · active matter · entangled matter · actuators · stimuli-responsive polymers · soft robotics

---

\*Corresponding author. Email: taylor.ware@tamu.edu

## 1 Introduction

Materials capable of self-assembly and disassembly in response to external cues hold promise to enable new functionality across engineering disciplines [1–3]. Such autonomous behaviors may offer novelty in fabrication and processing practices of bulk functional material, as well as in soft robotics, in which a swarming behavior of individual units can be manipulated to result in a stable solid structure [3, 4]. If such structures do not possess long range order (amorphous), they may further hold the benefit of requiring low levels of control over the assembly process to produce a multitude of forms with consistent properties [5, 6].

One interesting approach towards building materials that self-assemble and disassemble is to rely on interactions between units that are able to move independently. The general term used for such systems is active matter. Such systems are composed of individual active units (across a variety of scales) that are far from equilibrium, which consume energy to generate motion or mechanical work [7, 8]. In many cases, the propelling of individual elements drives the self-assembly of the units into a structure or aggregate leading to collective behavior and emergent properties. If the cohesive forces between the aggregate elements are a result of the continuous supply of energy to the elements, the structure will break down upon consuming the source or the cutoff of the energy supply. In some cases, collisions may result in jamming or entanglement which can lead to metastable assembly due to the frustrated interaction between the units [8, 9].

Some interesting sources of inspiration to cohesive interactions between active individuals that lead to collective mechanical behaviors can be found in the animal kingdom [8]. Notable examples are fire ants (*Solenopsis invicta*) [10], honeybees (*Apis mellifera*) [11], plant–animal worms (*Symsagittifera roscoffensis*) [12], and California blackworms (*Lumbriculus variegatus*) [13]. These species mechanically interlock (in response to environmental conditions) into cohesive masses that manifest various collective behaviors such as buoyant raft formation [14], colony unification [15] and thermal regulation [16]. By nature, these masses are porous structures with viscoelastic mechanical behaviors [17] that exhibit adaptive self-assembly and reorganization. These properties stem from each member’s ability to move within the confines of the structure, or in-and-out by physically detaching and reattaching to its neighbours [15, 18–20]. Moreover, their ability to reversibly transition between fluid- and solid-like states allows them to be uniquely adaptable and, as a mechanical system, to operate with a large number of degrees of freedom [21, 22]. In the context of a robotic system or a synthetic functional device made with a clear engineering application in mind, such capabilities have only been partially leveraged.

To-date, several synthetic realizations of interlocked aggregates have been realized. For example, a variety of granular and swarming robotic systems that self-assemble into two dimensional aggregates using loose magnetic coupling have been proposed. These systems were able to demonstrate transitions between collective states with solid- and liquid-like properties [4] and exhibited emergent collective properties such as locomotion and transport [23, 24]. However, this approach uses bulky robotic components, each requiring relatively complex integrated electronic circuits and controls. Other approaches employ the unique attributes of responsive polymeric materials. The use of polymeric materials can greatly enhance the simplicity of the responsive unit. Abdelrahman et al. [6] demonstrated the creation of transient viscoelastic aggregates from a range of functional polymer ribbons. Such materials included liquid crystal elastomers (LCE) which are loosely crosslinked responsive polymer networks that reversibly change their shape in response to external stimuli such as heat or light. However, the aggregation required a temperature transient and large concentrations of overlapping entangling units for aggregate formation.

In this work, we describe an approach to create transient, responsive solids from dilute suspension of mobile shape-changing polymeric ribbons. Specifically, we utilize the large-scale motion (i.e., much greater than a single body length) exhibited by magnetic and shape changing LCE ribbons in response to a rotating uniform magnetic field. When heated, ribbons change shape with prescribed amounts of bending and twisting, Figure 1a. Then, the rotation of the magnetic field induces aggregation through the entanglement of individual ribbons together into clusters, e.g., Figure 1b and Supplementary Video S1. We describe the thermal and magnetic response of individual ribbons, and track the aggregation kinetics of ribbon dispersions. Following the rotation of the magnetic field at elevated temperatures (65 °C, Figure 1c), the aggregates have a greater storage modulus than loss modulus up to shear strains of approximately 3%, constituting a solid-like behaviour, Figure 1d. The viscoelastic mechanical and rheological properties of the formed aggregates are found to vary with the single unit shape. Finally, we examine the critical conditions required for controlled aggregate disassembly.

## 2 Results and discussion

### 2.1 Thermal and Magnetic response

LCE ribbons that respond to heat by changing shape and respond by moving in an external magnetic field were fabricated. The response to the magnetic field is conferred via a composite LCE domain at the edge of the ribbon

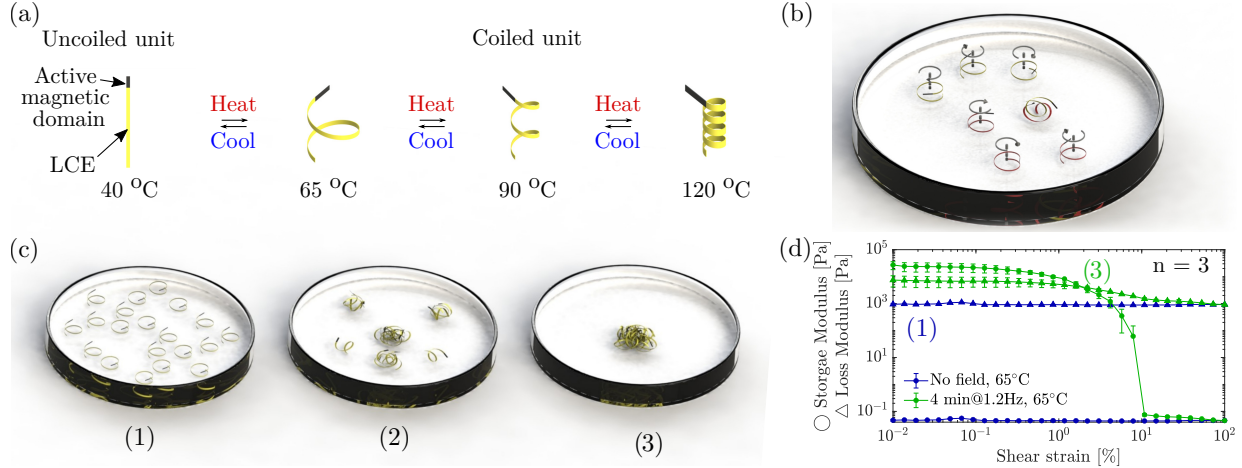


Figure 1: Schematic illustrating the mechanisms that drive shape change and entanglement in magnetically active LCE ribbons. (a) An initially straight ribbon undergoes an increasing amount of bending and twisting upon heating as a result of nematic-isotropic transition. (b) Schematic of thermally actuated ribbons undergoing axial rotation and lateral motion in a rotating magnetic field that results in entanglement. (c) A group of dispersed ribbons (1) undergo entanglement into smaller clusters (2) that eventually connect into a single aggregate (3). (d) Oscillatory rheological strain sweeps plotting the storage (round marker) and loss (triangular marker) modulus as a function of shear strain of ribbons with a length of 16 mm and offset angle  $\theta = 10^\circ$  before (1) and after (3) the application of the magnetic field. Error bars represent the standard deviation,  $n = 3$ .

filled with magnetic particles, Figure 1a and Supplementary Figure S1. The remainder of the LCE ribbon is shape responsive. The nematic director rotates by  $90^\circ$  through the film thickness (twisted nematic, Figure 2a), and heating causes the ribbon to morph from flat to 3D shapes with controlled degrees of bend and twist [25, 26]. Grazing incidence WAXS measurement on monodomain nematic film samples (uniform through the thickness) validated a high degree of molecular alignment along the prescribed orientation (Figure S1). The thermally induced transition from the nematic phase towards the isotropic phase locally induces a contraction along the nematic director that is accompanied by an expansion in the perpendicular direction. The amount of contraction is prescribed by the change in temperature. The most shape change occurs when heating above the nematic to isotropic transition temperature,  $T_{NI}$ . Twisted nematic ribbons with the nematic director at each face offset by an angle  $\theta$  to the principal axes of the ribbon, Figure 2b, exhibit controlled bending and twisting [25, 26]. The evolution of curvature with temperature for ribbons cut at different offset angles is shown in Figure 2d, and the amount of twist (around the long axis of the ribbon) per unit length at different temperature is shown in Figure 2e. Ribbons that were not cut at an offset angle,  $\theta = 0^\circ$ , only bend, show an approximately linear rate of increase in curvature of approximately  $0.014 \text{ mm}^{-1}/\text{C}$ . As expected, increasing the offset angle  $\theta$  shows a decrease in curvature and an increase in the amount of observed twist. Mild offset angles of  $\theta = 10^\circ$  showed similar curvatures to  $\theta = 0^\circ$  with an increased amount of twist. The twisting of the ribbon gives rise to a helical shape, Figure 2b, with the pitch proportional to the amount of twist. Specifically, for a 16 mm ribbon at  $65^\circ\text{C}$ , there is a quarter twist along the long axis of the ribbon. As temperature increases towards  $T_{NI}$ , the curvature of the ribbon increases, Figure 1a. Thus, the coil becomes tighter with decreases in pitch, length, and diameter.

Once the ribbon has acquired its actuated shape under the prescribed temperature, rotation of an external magnetic field is applied to induce the motion of the ribbon. The motion of the ribbon is a result of multiple factors including the magnitude of the magnetization in the ribbon, the external magnetic field, the geometry of the ribbon, and the viscosity of the media.

Magnetic actuation of different ribbon shapes, caused by heating to different temperatures, induces trajectories that vary in space and time (Supplementary Figure S2 and Supplementary Video S2). To obtain a measure of the response of ribbons to an applied rotating field, the position of the magnetic domain was tracked in time in the  $x - y$  plane (parallel to the fluid surface). The collected trajectories were filtered to a small range around the magnetic field rotation frequency, i.e., approximately 1.2 Hz or 72 RPM.

The measured actuation paths of the ribbons consist of repeatable patterns that indicate three distinct motion regimes. The first pattern is characterized by many acute-angled features,  $40^\circ\text{C}$  in Figures 2f-h. In this regime the ribbon frequently changes its direction of motion. The magnetic domain proceeds in a side-to-side flapping-like motion (e.g., Supplementary Video S2). This pattern of motion typically occurs when the ribbon is flat, and the magnetic

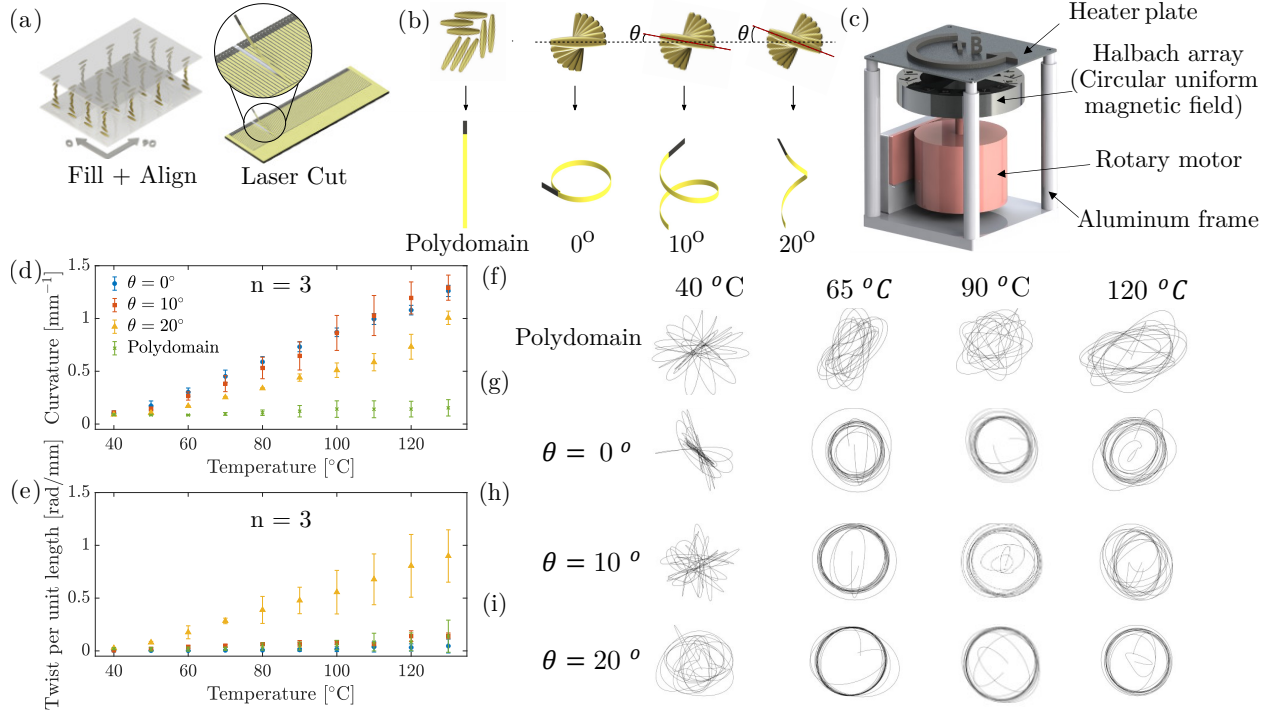


Figure 2: Characterization of thermal and magnetic actuation of single LCE ribbons. (a) Schematic of the fabrication process of a twisted-nematic LCE ribbon with a magnetic head. (b) Schematics of actuated LCE ribbons cut at different offset angle,  $\theta$ , relative to the surface nematic director, resulting in varying amounts of bending and twisting. (c) Schematic of the temperature controlled rotating uniform magnetic field. (d) Quantitative characterization of the amount of curvature as a function of temperature for ribbons with different offset angle,  $\theta$ . (e) Quantitative characterization of the amount of twist per unit length as a function of temperature for ribbons with different offset angle,  $\theta$ . (f)-(g) Fourier-filtered motion paths obtained by tracking the trajectory of the active head under a 72 RPM field rotation for polydomain,  $\theta = 0^\circ$ ,  $\theta = 10^\circ$ , and  $\theta = 20^\circ$  ribbons, respectively. In all panels, error bars represent the standard deviation,  $n = 3$ .

moment is unable to make the ribbon bend or rotate about its axis before the external field completes a full rotation. The second motion regime is more circular, 65 °C-120 °C in Figures 2g-i, indicating that on the time scale related to the magnetic field rotation, the ribbon is able to follow the field without changing directions (e.g., Supplementary Video S2). The third motion regime contains more relaxed angular features oriented in different directions 65 °C-120 °C in Figure 2f. This pattern indicates a transition regime in which the ribbon is able to partially follow the field rotation but still displays a sizeable, albeit smaller, amount of direction changes per rotation cycle.

We hypothesize that the conditions required for successful entanglement in our system are twofold. First, the ribbon should be able to successfully follow the field to maintain synchronicity with its cyclic trajectories. Such trajectories are typically represented by the more circular patterns, 65°C-120 °C in Figures 2g-i. Second, the ribbon should have a moderate amount of curvature that will allow ribbons to physically interlock with each other but not restrict interaction.

## 2.2 Assembly and aggregation kinetics

Magnetic actuation of many curved ribbons in a fluid induces isothermal aggregate assembly from dispersed states. In each of the following experiments, forty ribbons were initially placed in a dish filled with viscous silicone oil, corresponding to a LCE packing density of  $0.002 \text{ mg/mm}^3$ . The ribbons were placed in the oil such that there was no overlap between them ( $t = 0$ , Figure 3a). The motion induced by the magnetic field at low rotation speeds (72 RPM) facilitated entanglement of pairs of individual ribbons. Pairs subsequently grew into clusters through the annexation of additional ribbons or ribbon clusters, Supplementary Video S1.

Aggregation varies based on unit shape which is prescribed by the temperature. Time lapse images of dispersions of ribbons cut at ( $\theta = 10^\circ$ ) at different temperatures show different aggregation behavior, Figure 3a. At all temperatures

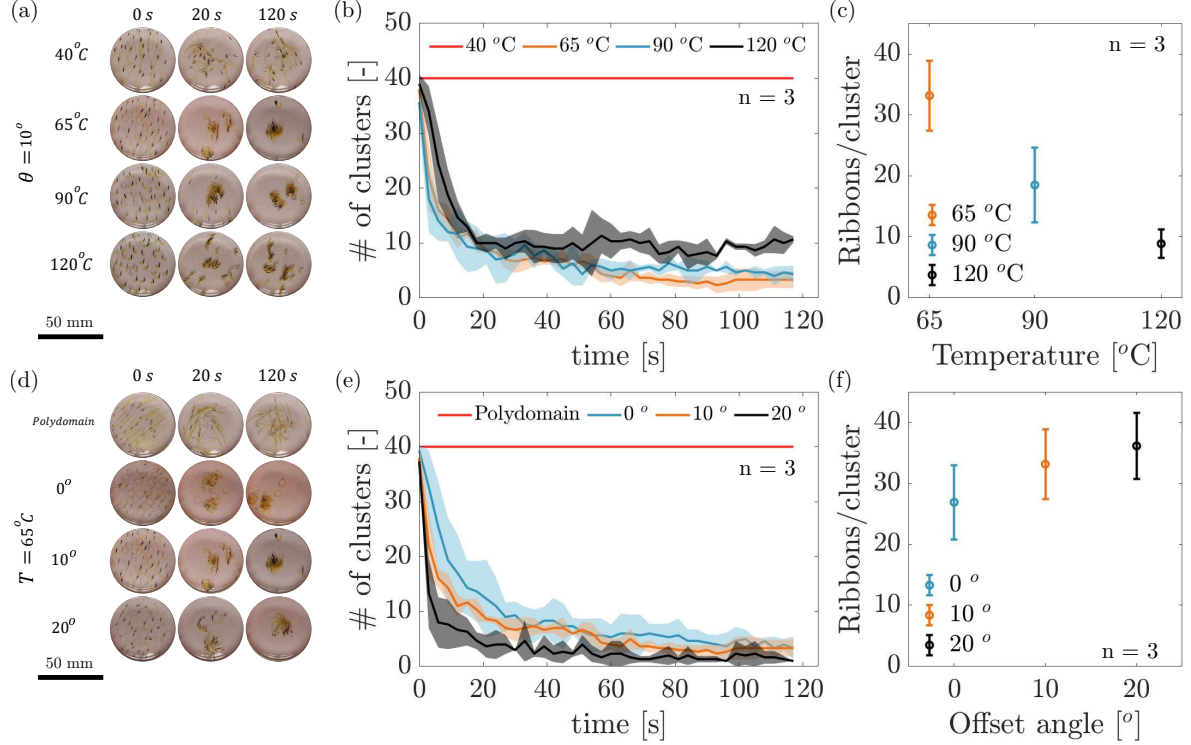


Figure 3: Ribbons entangle based on their shape. (a) Time lapse of the entanglement process for different ribbon shapes at different temperatures, taken at  $t = [0, 20, 120]\text{s}$ .  $\theta = 10^\circ$  ribbons at different temperatures. (b) Time evolution of the entanglement process for  $\theta = 10^\circ$  ribbons at different temperatures. Shaded region represent the standard deviation,  $n = 3$ . (c) Average number of ribbons per cluster after 120 s following the experiment presented in (b). Error bars represent the standard deviation,  $n = 3$ . (d) Time lapse of the entanglement process for different ribbon shapes at different temperatures, taken at  $t = [0, 20, 120]\text{s}$ . Different ribbon shapes at  $65^\circ\text{C}$  based on the fabrication process: polydomain, and offset cutting angle. (e) Time evolution of the entanglement process for ribbons with different offset angle  $\theta$  at  $T = 65^\circ\text{C}$ . Shaded region represent the standard deviation,  $n = 3$ . (f) Average number of ribbons per cluster after 120 s following the experiment presented in (d). Error bars represent the standard deviation,  $n = 3$ .

that induce shape change, aggregation is observed. At a common actuation temperature of  $65^\circ\text{C}$ , ribbons that bend and/or twist aggregate while those that remain flat (polydomain) do not. The time evolution of the # of clusters for offset angle  $\theta = 10^\circ$  at different temperatures ( $T = [65, 90, 120]^\circ\text{C}$ ) is presented in Figure 3b. At  $40^\circ\text{C}$  (red line), the ribbons remained flat and exhibited discontinuous flapping motion, similar to the motion pattern exhibited by single ribbons in Figure 2h. The lack of bending means no aggregation is observed (Figure 3a and Supplementary Video S3).

Aggregation kinetics vary at different times. At higher temperatures, aggregation time scale was not apparently different between different temperatures (or coil shape). The # of clusters decreases to below 25% of the initial number of ribbons within the first 20 s (early times) for all systems. Following the steep decline, aggregation occurs more slowly, eventually tending to an apparent steady state within 100 s (late times). During this time, collisions continue to happen between the formed clusters leading to the emergence of two main behaviors. The first behavior includes systems that did not achieve a steady state # of clusters smaller than 10% of initial units. Such systems, e.g.,  $\theta = 10^\circ$ ,  $T = 120^\circ\text{C}$ , exhibited repeated attachment and detachment events tending to a fluctuation around the late-time value, Figure 3b. The second behavior includes systems that achieved a steady state # of clusters smaller than 10% of initial units, favoring entanglement into large clusters. In these systems, the collisions resulted in the coalescence of the clusters through interactions between the dangling edges of different clusters, or the annexation of individual ribbons toward subsequent cluster growth,  $\theta = 10^\circ$ ,  $T = 65^\circ\text{C}$  in Figure 3a.

A low number of resulting clusters provides an indication of ‘successful’ entanglement. However, to determine which of the above scenarios occurred, it is important to account for the distribution of cluster sizes. To account for this measure, we can consider the average number of ribbons in each cluster. The weighted average cluster size in the experiments presented in Figure 3b ( $\theta = 10^\circ$ ,  $T = [65, 90, 120]^\circ\text{C}$ ) is presented in Figure 3c. The  $\theta = 10^\circ$ ,  $T = 90^\circ\text{C}$  ribbon system exhibited a late-time value of  $4 \pm 2$  clusters which had an average cluster size of  $18 \pm 5$  ribbons/cluster,

this constitutes a yield of merely 45% of the initial number of ribbons. The  $\theta = 10^\circ$ ,  $T = 65^\circ\text{C}$  exhibited a late-time value of  $3 \pm 1$  clusters which had an average cluster size of  $34 \pm 4$  ribbons/cluster, constituting a 85% yield of the initial number of ribbons. This is also evident from time lapse images presented at the rightmost column ( $t = 120$  s) of Figure 3a. Thus, a cluster size approaching the initial number of units will indicate a successful entanglement that has resulted in the formation of a single mass.

Ribbons with moderate curvature form larger aggregates. At  $65^\circ\text{C}$ , the average number of ribbons per cluster is greatest with an average yield of approximately 85%. This indicates that the moderate amount of curvature exhibited by the ribbons at moderate temperatures is more favorable for promoting entanglement as compared to the high curvature, tightly coiled shapes found at higher temperatures near  $T_{NI}$ . We expect that the relatively low curvature enables interaction that results in the interlocking of the ribbons. Additionally, the tightly coiled high temperatures conformations at  $90^\circ\text{C}$  and  $120^\circ\text{C}$  do not supply the formed aggregates with ‘loose’ edges that facilitate growth through coalescence with other clusters or ribbon annexation.

The shape of ribbons at a common temperature resulting from varying the offset angle is also expected to affect aggregate formation. We consider three different actuated shapes based on varying the offset angle,  $\theta = [0^\circ, 10^\circ, 20^\circ]$ , exhibiting different amounts of curvature and twist. As a control, we consider a polydomain ribbon, which does not exhibit any actuation (i.e., remains flat) at elevated temperature. Time lapse images of dispersions of ribbons with different shapes at  $65^\circ\text{C}$  are shown in Figure 3d. The time evolution of the # of clusters for different offset angles at  $65^\circ\text{C}$  is presented in Figure 3e, and the average number of ribbons per cluster is presented in Figure 3f. Again, the flapping motion performed by the polydomain ribbons (red line) did not result in any bending from the ribbons (Supplementary Video S3) which did not result in entanglement.

The kinetics of aggregation of different ribbon systems that aggregate did not exhibit any discernible differences. Although some variation is apparent, no substantial difference in kinetics or average cluster size was observed between the different angles at  $65^\circ\text{C}$ . In all systems, two aggregation rates were observed, a fast drop in # of clusters lasting approximately 20 s followed by a slower decrease lasting approximately 80 s. In all systems, the formed aggregates occupied a volume approximately 80-90% smaller than in their dispersed state, Figure S3. This indicates that a continuous motion in circular patterns does result in successful entanglement. Similar observations were further reported by Patil et al. [13] in a computational study of active filaments representing dynamic reversible entanglement in the California blackworms. The evident considerable entanglement achieved in all systems in which the two of our preliminary conditions are fulfilled, i.e., continuous synchronicity with the field rotation and moderate curvature, can be considered to support our preliminary hypothesis.

### 2.3 Mathematical model for dynamic entanglement

By developing a mathematical model for the ribbon dynamics we can identify the governing mechanisms underlying the aggregation process. In particular, this model allows us to understand the role of topological and non-topological mechanisms in aggregation. Our model treats the ribbons as rigid filaments moving in a cylindrical domain with diameter  $3.8L$  and height  $L$ , where  $L$  is the length of a ribbon. To promote entanglement, the process is started from a random initial condition in which the center of mass of each ribbon is in the same plane. Each ribbon then experiences constant driving torques, analogous to the forces on the magnetic domain in the LCE ribbons, along with an external stochastic drift force. The ribbons also feel contact forces and torques arising from their interactions [27, 28] (Supplementary Information, Supplementary Video S4). These contact forces typically include an adhesion term which prevents touching ribbons from separating unless their separation force exceeds a critical value. To understand how topological and non-topological parameters govern the aggregation process, we vary filament shape (Figure 4a; top row and bottom row) and adhesion strength (Figure 4a-c and Figure 4d-f).

Filaments of different shapes exhibit different propensities to entangle with other, and thus help illustrate how topology affects aggregation. Here, two filament shapes are considered: a low curvature shape, corresponding to  $\theta = 10^\circ$  ribbons at  $65^\circ\text{C}$  (Figure 4a, top row), and a high curvature shape, corresponding to  $\theta = 10^\circ$  ribbons at  $90^\circ\text{C}$  (Figure 4a, bottom row). When adhesion forces are switched on, and the filaments are ‘sticky’, these different shapes give rise to strikingly different aggregation dynamics (Figure 4b) which resemble the experimental results in Figure 3b.

To understand the topological origin of this difference, we introduce the excess linking per filament (Figure 4c), which quantifies the entanglements in a multi-filament system. This quantity is built out of the open linking number,  $Lk_{ij}^O$ , which captures pairwise entanglement between the  $i$ ’th and  $j$ ’th filament [13, 29]. For  $N$  filaments, the excess linking per filament is the average amount of linking with a single filament, relative to the average amount of linking found in a random configuration of filaments (Supplementary Information). At  $200T_0$ , the low curvature filaments exhibit a much more robust amount of entanglement than the high curvature filaments, as expected from their larger cluster sizes (Figure 4b). Previous work has indicated that an open linking number with magnitude 1/2 approximately

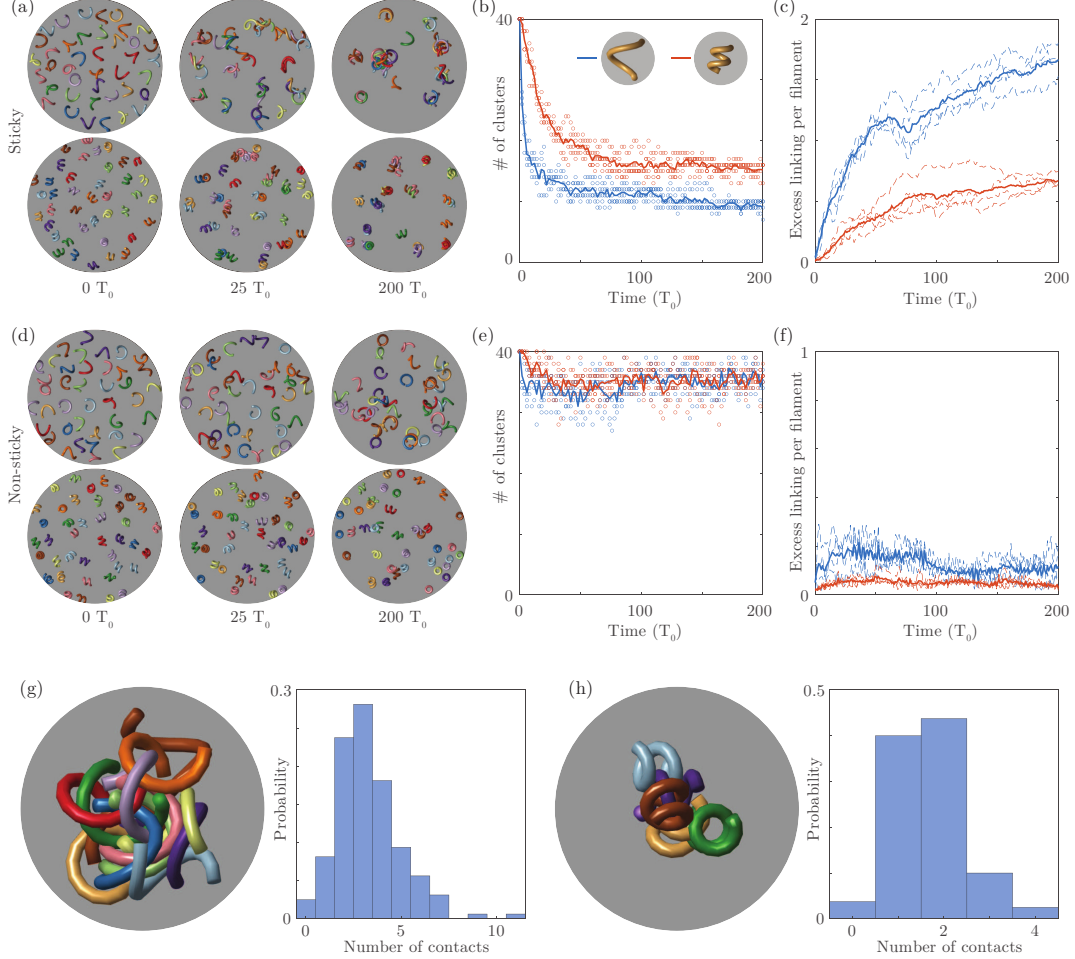


Figure 4: Simulations reveal the topological and non-topological aspects of filament aggregation. (a) Time-lapse images from simulations of ‘sticky’ filaments (Supplementary Information) exhibit aggregation, starting from a randomly chosen initial state. Filament shapes correspond to  $\theta = 10^\circ$  at  $65^\circ\text{C}$  [top row] and  $90^\circ\text{C}$  [bottom row]. (b) Fewer clusters containing larger numbers of filaments are formed by the  $65^\circ$  filaments (blue), demonstrating their increased capacity for entanglement relative to the  $90^\circ$  filaments (red). Circles show individual simulations, solid curves show mean values ( $n = 4$ ). (c) Entanglement, as measured by excess linking per filament (Supplementary Information), illustrates the topological distinction between the  $65^\circ\text{C}$  and  $90^\circ\text{C}$  filaments. Dashed curves show individual simulations, solid curves show mean values ( $n = 4$ ). (d) Time-lapse images from simulations of ‘non-sticky’ filaments (top row:  $65^\circ\text{C}$ ; bottom row:  $90^\circ\text{C}$ ). (e) Large clusters do not form for either the  $65^\circ\text{C}$  filaments (blue) or the  $90^\circ\text{C}$  filaments (red). Circles show individual simulations, solid curves show mean values ( $n = 4$ ). (f) Excess linking per filament (Supplementary Information) is close to 0, demonstrating that ‘non-sticky’ filaments suppresses the topological effects of (c). Dashed curves show individual simulations, solid curves show mean values ( $n = 3$ ). (g) Cluster of  $65^\circ\text{C}$  filaments in the ‘sticky’ case (left). The relatively large observed number of contacts for a given filament at time  $200T_0$  in simulation (right) explains the size of the cluster. (h) Cluster of  $90^\circ\text{C}$  filaments in the non-sticky case (left). The small observed number of contacts (right) limits the aggregation process.

matches an intuitive notion of entanglement between two filaments [13]. Since the high curvature filaments achieve an excess linking per filament of approximately  $1/2$  (Figure 4c), this suggests that these filaments effectively pair off into clusters of size 2. This is consistent with the cluster number results (Figure 4b), which show the high curvature filaments forming  $\approx N/2$  clusters from  $N$  initial filaments.

The time evolution of the excess linking per filament additionally provides information on the end-state of the aggregation process. In particular, this order parameters appears to have a positive late-time slope for all filaments in Figure 4c. This indicates that although the number of clusters is approximately constant beyond  $100T_0$ , there is a continued, albeit slower, growth in cluster size during this time. Additionally, this rate of growth is much faster for

lower curvature filaments, indicating a higher propensity for entanglement, in agreement with the experimental data in Figure 3b and Figure 3c.

In addition to topological entanglements, the non-topological adhesion forces themselves play a pivotal role in the assembly of the aggregate (Figure 4d). A representative time-lapse of simulations for ‘non-sticky’ (Supplementary Information) low and high curvature filaments are shown in Figure 4d (see also Supplementary Video S4). In this scenario, the filaments behave as smooth objects that are devoid of any cohesive interactions. As a result, their cumulative entanglement is solely due to topological interactions. Importantly, the time evolution of the # of clusters in the ‘non-sticky’ case (Figure 4e) is drastically different than that of the ‘sticky’ case (Figure 4b). At early times ( $t < 25T_0$ ), a very small decrease in the # of clusters is apparent, however both filament types have cluster numbers above 80% of their initial number. The system then maintains an approximately constant rate of neutral collisions which do not lead to entanglement-induced aggregation. This picture is further supported by the excess linking per filament (Figure 4f), which approaches zero at late times, indicating the absence of meaningful aggregation. The fact that the excess linking does not reach zero is due to the choice of initial state (Supplementary Information) and indicates that the process has not fully equilibrated. Notably, the large initial spike in the excess linking per filament for low curvature filaments further demonstrates their higher innate propensity for topological entanglement.

The structure of the clusters formed in simulation can be analyzed in more detail. Following an extended simulation time, low curvature filaments form larger aggregates (Figure 4g) than those formed using high curvature filaments (Figure 4h). The distribution of the number of contacts for low curvature filaments in an aggregate takes larger values than the contact distribution for high curvature filaments. This again illustrates that in large aggregates, low curvature ribbons can form a larger amount of connections, providing a mechanism for aggregate growth. Since the capacity for high curvature filaments to connect saturates faster, continued collisions may result in non-constructive interactions that explain the lower slope in Figure 4c. The above results could be used to further control the self-assembly of clusters with designer geometric and topological properties.

## 2.4 Mechanical properties of the aggregate

The fluid-like dispersions of ribbons aggregate into solid collectives. The combination of the high aspect ratio of the ribbon geometry and the induced curvature enable the ribbons to entangle and interlock to form physical bonds. The formation of such bonds drives a transition from a liquid dispersion into a solid mass. To confirm the successful formation of a solid phase, oscillatory strain sweep tests of ribbons in silicone oil were carried out using shear rheometry (Figure 5a and Figure 5b). All testing on aggregates was performed following the application of a magnetic field at 72 RPM for 4 minutes from an initially dispersed state ( $t = 0$  in Figure 3a). Both storage and loss moduli increase with increased deformation frequency ( $\theta = 10^\circ$  aggregates formed at 65°C, Figure 5c). Such a rate dependent response of the material is indicative of viscoelastic response. Control measurements were taken in which no ribbons were present in the oil (black lines) and with the ribbons placed in the original dispersed state without the prior activation of the magnetic field (gray lines), Figure 5d. The oil and the dispersion of unentangled ribbons each behaved as liquids with moduli dramatically lower than the moduli of the entangled aggregates, Figure 5d and Figure 1d. We report the moduli of the dispersion normalized to the entire plate geometry, despite the fact that if an aggregate forms, the region that contains ribbons is smaller than the plates.

The aggregates have the properties of viscoelastic solids. At 65°C (Figure 5d and Figure 5e) all entangled samples exhibited a viscoelastic behavior that included a linear viscoelastic region at small shear strain values ( $\lesssim 0.1\%$ ) with both storage and loss moduli at least one order of magnitude larger than those measured for the controls. At higher strain values, a transition to fluid-like behavior is observed by the increase of the loss modulus over the storage modulus. This was followed by a sharp decrease of the two moduli tending to the behavior of the pure viscous oil solution, indicating the dissociation of the aggregate.

The storage modulus of the aggregate depends on the actuated ribbon shape. Namely, ribbons that bend ( $\theta = 0^\circ$ , blue lines) and ribbons that bend and mildly twist ( $\theta = 10^\circ$ , green lines) resulted in aggregates with larger stiffness relative to aggregates formed from ribbons with a higher twist per length,  $\theta = 20^\circ$  in red (cf. Figure 5e and Figure 2). This finding is consistent with measurements taken for LCE ribbon systems formed through static aggregation (i.e., only thermal actuation from an initially overlayed state) performed by Abdelrahman et al. [6]. However, Abdelrahman et al. [6] found purely bending ribbons to form slightly stronger aggregates than those that coil, when formed statically. Our data provide some evidence to support the postulate that coils with a mild twist facilitate better dynamic entanglement by enabling tight assemblies of interlocked ribbons through interweaving rotational motion. A similar mechanism was also identified by Patil et al. [13] for the dynamic entanglement of the California Blackworm.

Entanglement at increased temperatures (or tighter coil conformations) reduces the yield stress of the formed aggregates, cf. Figure 3b,c. The storage and loss modulus of mildly coiled,  $\theta = 10^\circ$ , ribbons are presented in Figure

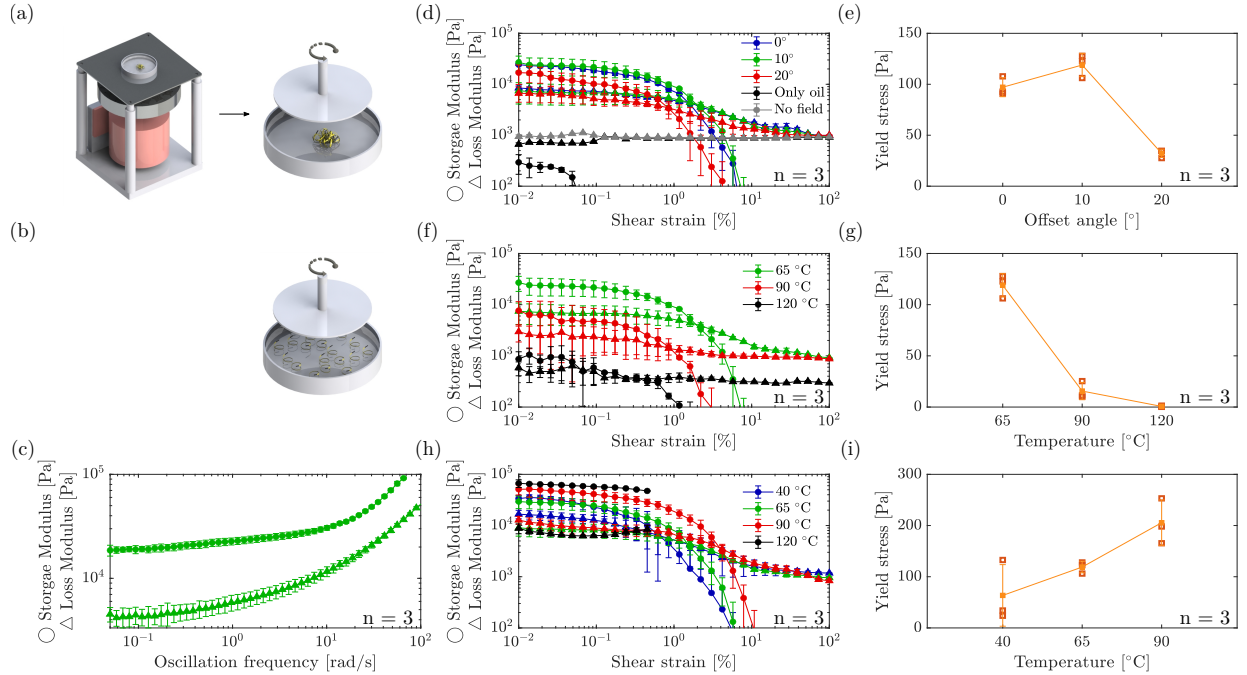


Figure 5: Rheological properties of ribbon aggregates. (a) Schematic of experimental procedure. The ribbons are entangled in the magnetic field and are then subjected to a rheological sweep using a parallel plate geometry inside a submerged well of silicone oil. (b) Schematic of control procedure. The ribbons are dispersed in a well of silicone oil without the application of a magnetic field and are then subjected to a rheological sweep using a parallel plate geometry. (c) Frequency sweep of entangled aggregates of 40  $\theta = 10^\circ$  ribbons at  $T = 65^\circ\text{C}$ . (d) Strain sweep of entangled aggregates of 40 ribbons with different offset angle  $\theta = [0, 10, 20]^\circ$  at  $T = 65^\circ\text{C}$ . (e) Yield stress values extracted from the respective rheological sweep in (d). (f) Strain sweep of aggregates of 40  $\theta = 10^\circ$  ribbons entangled at different temperatures,  $T = [65, 90, 120]^\circ\text{C}$ , and tested at the formation temperature. (g) Yield stress values extracted from the respective rheological sweep in (e). (h) Strain sweep of aggregates of 40  $\theta = 10^\circ$  ribbons entangled at  $T = 65^\circ\text{C}$  and tested at different temperatures,  $T = [40, 65, 90, 120]^\circ\text{C}$ . (i) Yield stress values extracted from the respective rheological sweep in (h). In all panels, Error bars represent the standard deviation,  $n = 3$ .

5f ( $n = 3$ ). There is a sharp decrease in both the storage modulus and the yield stress for aggregates formed at  $90^\circ\text{C}$  (Figure 5g). Only weak aggregation is observed for aggregates formed at  $120^\circ\text{C}$  (approximately tending to the behavior of pure oil, Figure 5e). This weak aggregation is in agreement with the reduction in aggregate size in Figure 3c. We expect that tightly coiled individual ribbons do not entangle efficiently. Thus, collision events result in destructive/neutral effects rather than aggregation.

Heating aggregated samples can increase bond strength within the aggregate. Aggregates of ribbons are formed at  $65^\circ\text{C}$ , in the same way as described above. The testing of the aggregate occurs at different temperatures ( $\theta = 10^\circ$ , Figure 5h,  $n = 3$ ). We expect that the increase in curvature induced by the thermal actuation above the aggregation temperature will increase the bond strength and possibly also the number of bonds between ribbons. The red line indicates samples that were entangled at  $65^\circ\text{C}$  and subsequently cooled down to the crosslinking temperature,  $40^\circ\text{C}$ , in which isolated ribbons return to their flat conformation. In large volumes of oil, the aggregate flows and partially redisperses. When the aggregate is placed in the rheometer and allowed to cool, macroscopic flow was not obvious (Supplementary Video S5). The cooled samples exhibit a similar storage modulus to that obtained at  $65^\circ\text{C}$  with an increased loss modulus throughout the linear viscoelastic region, which implies higher energy dissipation through viscous flow. Samples tested at  $40^\circ\text{C}$  have a decreased yield strain as compared to samples tested at  $65^\circ\text{C}$ . Increasing temperature after aggregation resulted in changes to aggregate dimensions (Supplementary Figure S4) for which gap heights were appropriately adjusted (section 4 for more details). At  $90^\circ\text{C}$  and  $120^\circ\text{C}$ , the aggregates possess higher storage moduli and yield stresses. The increases in moduli and yield stress (Figure 5i) signify increases in both aggregate rigidity and bond strength. The data from the  $120^\circ\text{C}$  (black line) experiment is only plotted up to the approximate end of the linear viscoelastic region as dissociation was not observed and slipping occurred.

## 2.5 Disassembly of aggregates

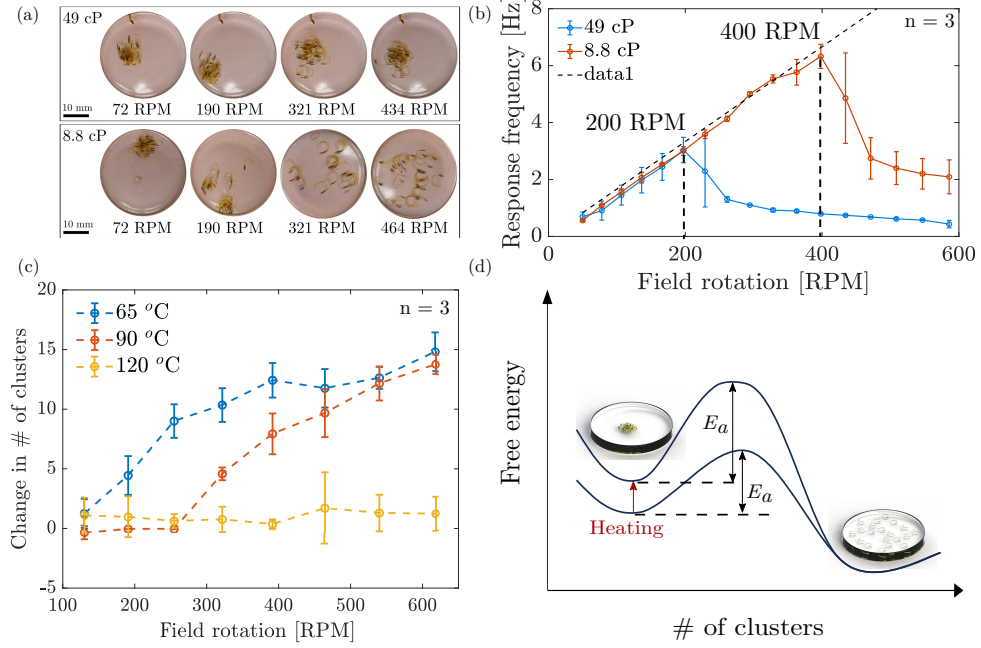


Figure 6: Dissociation dynamics of ribbon aggregates. (a) Dissociation of  $\theta = 10^\circ$  ribbons at  $T = 65^\circ\text{C}$  in a 49 cP ([top panel]) and 8.8 cP ([bottom panel]) silicone oil subjected to 1 minute magnetic field at different rotation speeds [72,190,321,434,464] RPM. (b) Rotational response frequency of the magnetic head as a function of different field rotation speeds for silicone oils with different viscosity. (The identified step-out frequency is marked by the dashed lines.) Error bars represent the standard deviation,  $n = 3$ . (c) Change in average number of  $\theta = 10^\circ$  ribbons as a function of field rotation at different temperatures,  $T = [65, 90, 120]^\circ\text{C}$ . Error bars represent the standard deviation,  $n = 3$ . (d) Schematic of the free energy barrier (represented by the activation energy,  $E_a$ ) required for dissociation of ribbon aggregates.

We hypothesized that aggregate disassembly can be induced through magnetic field rotation at high speeds. However, in moderately high viscosity oil ( $\eta = 49$  cP), an entangled aggregate that was subjected to increasingly high rotation speeds of the field did not result in the dissociation of the aggregate, top panel in Figure 6a. Above a critical frequency, magnetic field rotation resulted in vibration of the magnetic domain, indicating that the rotational kinetic energy did not transfer to the ribbon, Supplementary Video S6. This loss of synchronicity is due to the critical ‘step-out’ frequency, representing the threshold above which the applied magnetic torque is not strong enough to keep the ribbon synchronized with the field [30]. The step-out frequency can be controlled with the ribbon magnetization, viscosity of the environment, and the external field strength.

The viscosity of the oil surrounding the ribbons is critical to isothermal aggregate dissociation. The average step-out frequency of a single ribbon ( $\theta = 10^\circ$ ) at  $65^\circ\text{C}$  in a room temperature viscosity of  $\eta = 49$  cP oil was found to be approximately 200 RPM, Figure 6b ( $n = 3$ ). However, a 5.6-fold decrease in a room temperature viscosity ( $\eta = 8.8$  cP) yielded a two-fold increase in the step-out frequency to 400 RPM, Figure 6b ( $n = 3$ ). The step-out frequency was taken as the point in which the response curve departs from the line representing where response frequency equals field rotation frequency (dashed line). When applying increasing field rotation speeds on an entangled aggregate in low viscosity oil ( $\eta = 8.8$  cP), one minute exposures resulted in an increasing degree of dissociation, bottom panel in Figure 6a. To quantitatively explore the process kinetics, we tracked the evolution of the # of clusters in time over one minute. Similarly to association kinetics, the majority of the transient process ended after approximately 20 s (Supplementary Figure S5), and the # of clusters was averaged over the final 30 second ( $n = 5$ ).

The critical threshold for dissociation depends on the aggregate bond strength. The # of clusters at different magnetic rotation speeds for aggregates formed at  $65^\circ\text{C}$  in  $\eta = 8.8$  cP oil and heated to three different temperatures,  $T = [65, 90, 120]^\circ\text{C}$  is presented in Figure 6c ( $n = 3$ ). The curves indicate that dissociation into clusters becomes substantial only above approximately 200 RPM at  $65^\circ\text{C}$  and that the amount of dissociation increases with the increase

in supplied rotational energy. An approximate plateau is reached around 400 RPM (i.e., the step-out frequency obtained for  $\eta = 8.8$  cP).

Aggregates entangled at 65°C but tested at increased temperatures show a shift in the magnetic field rotation speed (or activation energy) required for cluster dissociation, as represented by the schematic in Figure 6d. For example, at 90°C, the minimal frequency for dissociation to occur was approximately 320 RPM, and for 120°C there was no effective dissociation, indicating that the critical barrier for dissociation is again higher than the given step-out frequency of 400 RPM.

The relative bond strength between ribbons can be estimated using the activation energy for dissociation. The activation energy,  $E_a$ , represents the minimal amount of rotational kinetic energy required to dissociate the physical bonds in the cluster. We can estimate bond strength using a linear regression (Supplementary Figure S6) to an Arrhenius-like model (Supplementary Information A.4). This measure was used to evaluate the critical magnetic field rotation speed,  $\omega_c$ . Aggregates at 65°C, were found to have an activation energy of dissociation  $E_a = 0.76$  nJ (95% CI: [0.69, 0.83] nJ), corresponding to  $\omega_c = 206.6$  RPM (95% CI: [197, 216] RPM). At 90°C aggregates were found to have  $E_a \approx 2.71$  nJ (95% CI: [2.33, 3.10] nJ), corresponding to  $\omega_c \approx 390.1$  RPM (95% CI: [361.4, 416.8] RPM).

### 3 Conclusion

We report a method to create macroscopic aggregates capable of autonomous assembly and disassembly. Liquid crystal elastomer ribbons are programmed to transition reversibly from flat to three dimensional shapes combining bending and twisting. A magnetic domain on the ribbon induces motion through an area much larger than the total length of the ribbon in response to an external, rotating, and uniform magnetic field. As the ribbons move, aggregation from dispersed states is observed. Repeated interactions create entangled clusters that grow over time. The aggregates retain their structure when the magnetic field is removed. The governing mechanisms that control these interactions, are studied using a mathematical model that explores their emergent collective topological dynamics. The model supports experimental evidence that the shape of the filaments affects the final size of the aggregate and demonstrates that cohesive forces play a pivotal role in the topological assembly of the aggregate. Namely, lower curvature filaments have a higher propensity for topological entanglement and are capable of forming a larger amounts of interconnections than the tighter, higher curvature filaments. This propensity, however, requires some additional cohesive interaction to be locked-in and facilitate growth. The formed aggregates are shown to exhibit the properties of viscoelastic solids that are able to store and dissipate energy, and the shape of the individual unit is shown to affect both the aggregation dynamics and the properties of the resulting aggregate. Additionally, we induce controlled dissociation through imparting kinetic rotational energy to the individual ribbons at high field rotation speeds. Ribbon shape and the medium in which dissociation occurs govern disassembly. In essence, slower motion of the ribbons enables the constructive entanglement of the ribbons, while higher velocity motion interferes with these processes and results in dissociation. In light of the mechanistic results from the model, the calculated activation energy for dissociation can be assumed to be related to the frictional energy between the aggregated ribbons. The individual motion apparent in both the constructive (assembly) and deconstructive (disassembly) mechanisms are reminiscent of the dynamic behaviors prevalent in aggregating systems in the animal kingdom, such as worms and fire ants. Imparting such abilities into synthetic systems may enable a wide range of materials to be assembled on demand, enabling a range of potential applications from bio-inspired soft robotics to injectable biomaterials.

### 4 Experimental Section

**Materials** Liquid crystal monomer 1,4-bis-[4-(6-acryloyloxyhexyloxy)benzoyloxy]-2-methylbenzene (RM82) was purchased from Henan Daken Chemical Co.,Ltd and monomer 1,4-bis-[4-(3-acryloyloxypropoxy)benzoyloxy]-2-methylbenzene (RM257) was purchased from Wilshire inc. KG. Photoinitiators Irgacure I-369 and Irgacure I-651, chain extender n-butylamine, dimethylformamide, toluene, acetone, isopropanol, silicone oil (49 cP) were purchased from Fisher Scientific. Low viscosity silicone oil (8.8 cP) was purchased from Clearco inc. Brilliant yellow dye was purchased from Chem-Impex inc. Neodymium-iron-boron (NdFeB) magnetic microparticles (average diameter = 25  $\mu\text{m}$ ) were purchased from Magnequench. A two-part polydimethylsiloxane (PDMS) elastomer was purchased from Ellsworth Adhesives. High temperature block magnets (BX088SH) were purchased from k&J Magnetics.

**Synthesis and Preparation** Clean glass slides (VWR) with dimensions of 38mm  $\times$  75mm  $\times$  1mm were subjected to O<sub>2</sub> plasma for 5 min. Subsequently, the slides were spin-coated with 1wt% brilliant yellow solution in dimethylformamide

at a spin speed of 1,500 RPM for 30 s. The slides were baked for 30 min at 100°C on a hotplate to ensure the evaporation of dimethylformamide. Each coated glass slide was exposed to linearly polarized broadband visible light from a modified projector at an intensity of 10 mW/cm<sup>2</sup> for 7 min to align the brilliant yellow molecules [31]. For the preparation of polydomain samples, no polarized light exposure was used. After alignment, the coated glass slides were spin-coated at a speed of 1,000 RPM for 15 s with a 9 wt% RM257 (reactive mesogens) and 1 wt% I-651 (photoinitiator) toluene solution (10 wt% solids). The slides were then irradiated with 365 nm ultraviolet (UV) light at an intensity of 2 mW/cm<sup>-2</sup> for 5 min using a UV oven (UVP Crosslinker CL-3000) for polymerization. Glass cells were prepared by adhering a pair of RM257-coated glass slides together using a 50 µm Kapton Polyimide film spacer (McMaster Carr) and superglue (Gorilla). A 1.4:1.0 molar ratio of RM82 to n-butylamine was heated and mixed with 1 wt% of I-369. The solution was then allowed to partially fill the glass cell through capillary action on a hotplate at 75 °C before placing it in an oven at 75 °C to complete the filling and oligomerization. After 15 h of oligomerization, the glass cells were allowed to cool to 40 °C temperature before exposing the cell to 365 nm UV light (Lumen Dynamics, OmniCure LX400+) at an intensity of 12 mW/cm<sup>-2</sup> for polymerization for 50 min on each side. After polymerization, an additional slide coated with brilliant yellow and polymerized RM257 (as mentioned above) was attached to the cell in the plane of one of the glass slides to create space for the magnetic domain. The slide was separated using a 100 µm Kapton Polyimide film spacer (McMaster Carr) and adhered to the cell using superglue. The formed space was filled with a 1.4:1.0 molar ratio of RM82 to n-butylamine with 20 wt% (NdFeB) magnetic microparticles and 1 wt% of I-369. An additional oligomerization cycle was performed as mentioned above before exposure to 365 nm UV light (Lumen Dynamics, OmniCure LX400+) at 40 °C under an intensity of 12 mW/cm<sup>-2</sup> for polymerization for 15 min on each side. After polymerization, the top glass slide was released, and the film was cut using a CO<sub>2</sub> laser cutter (Gravograph CO<sub>2</sub> laser LS100-40W). The cut ribbons were washed in water to remove brilliant yellow residue and the magnetic domains were magnetized under a 2.8 T impulse magnetic field (ACS Scientific IM-10-30). The twisted nematic ribbons were magnetized at an angle corresponding to the offset angle with respect to the long axis of the ribbon. Polydomain ribbons were magnetized in the direction parallel to the long axis of the ribbon.

**Temperature controlled rotating magnetic field apparatus** The apparatus frame was made from aluminium and constructed using a custom design. A uniform magnetic field was achieved by forming a circular Halbach array (Halbach cylinder,  $k = 2$ ) made from an aluminium frame housing 16 Nickel-coated high temperature block magnets (N42SH) with dimensions 1"×1/2"×1/2" arranged in a circle with a 115 mm diameter, Figure S7. The array was mounted on a 24V brushed DC Electric Motor. The bottom side of a thin aluminium plate with dimensions 150 mm×150 mm×2 mm was mounted with a 6" adhesive silicone rubber heater 120 VAC, 10 W/in<sup>2</sup> (35765K423, McMaster-Carr). The plate was mounted 15 mm above the Halbach array, resulting in an average field strength of approximately 20 mT in the plane of plate. The heater was connected to a Process PID controller (48VFL, EXTECH) powered by a variable AC voltage Transformer (TDGC-0.5KM, VEVOR) set to 94 V. The oil temperature was checked using a thermocouple (20250-91, Digi-Sense).

**Curvature and twist measurements** Curvature and degree of twist per unit length were measured by fixing a small (5 mm) piece of ribbon in place using a clip submerged in a temperature controlled oil bath. The induced curvature at different temperatures was evaluated by fitting a circle to the curved surface of the actuated ribbon. The degree of twist was evaluated by tracking the angle between the free end and the fixed end of the ribbon. Three separate batches of ribbons were tested for each condition.

**Video tracking and analysis** Videos of experiments were captured using a Canon Rebel T5i camera from top view. Tracking of the magnetic domain was conducted on 20 s videos taken at 60 FPS using a custom Matlab code. The code captured the  $x(t)$  and  $y(t)$  coordinates of the average center of the magnetic domain in time. To simplify the result and elucidate the features directly related to the magnetic field, the obtained time series were filtered using Matlab's 'Bandpass' subroutine in the range [0.5,1.4] Hz to attenuate lateral motions that occur on different time scales than that of the field rotation, set to 1.2 Hz or 72 RPM. Aggregation experiments were performed by capturing 2 min videos taken at 60 FPS. Analysis was applied on 40 frames taken at equal 3 s intervals by manual sampling of individual clusters and ribbons. Dissociation experiments were performed by capturing 1 min videos taken at 60 FPS. Analysis was applied on 10 frames taken at equal 6 s intervals by manual sampling of individual clusters and ribbons. To account for the effect of the viscosity, i.e., 'step-out' frequency, the motion of a single ribbon in the field was tracked in time at

different field rotation speeds. Then, the power spectrum of the signal was obtained using the Matlab ‘pspectrum’ subroutine, and the largest non-zero frequency peak value was considered for the rotational frequency response of the ribbon. Three separate batches of ribbons were tested for each condition.

**Rheological characterization** To measure the rheological properties of aggregates or dispersions, previously reported experiments were followed with modification [6]. Briefly, parallel-plate rheological scans were conducted utilizing a rheometer (Anton Paar Physica MCR 301). An aluminium well (50 mm diameter) was placed on the base to contain the ribbons and silicone oil in the rheometer (Figure 5). The oil temperature was checked using a thermocouple (20250-91, Digi-Sense). A consistent gap height of 3.5 mm was validated using the controlled rheometer displacement. Control experiments were performed in which no ribbons were placed in the oil (labeled ‘Only oil’) and in which the ribbons were dispersed in the way similar to the initial condition of the aggregation experiments (labeled ‘No field’), Figure 5b. Aggregates were formed by dispersing the ribbons in a dish and applying the field rotation at 72 RPM for 4 minutes. Then, the formed aggregate was manually transferred using tweezers to the preheated aluminium well mounted on the rheometer.

Oscillatory strain and frequency sweeps with a gap of 3.5 mm were performed for measuring the storage and loss moduli as a function of shear strain from 0.01% to 100.00% (at an angular frequency of 10 rad/s<sup>-1</sup>), and 0.05 rad/s to 100 rad/s (at 0.05% strain). Measurements taken at 90 °C were taken using a 3.35 mm gap height, approximately 4.5% lower than 3.5 mm, based on the average change in aggregate height associated with heating (Supplementary Figure S4). Measurements taken at 120 °C were taken using a 3.18 mm gap height, approximately 9% lower than 3.5 mm, based on the average change in aggregate height associated with heating (Supplementary Figure S4). The average changes in aggregate heights were obtained by measuring the dimension change relative to a submerged reference in a controlled oil heat bath. The yield stress and yield strain values were measured as the shear stress and strain value at the cross-over point between the loss modulus and storage modulus [32, 33]. Three separate batches of ribbons were tested for each condition.

**Grazing-incidence wide-angle X-ray scattering** Grazing-incidence wide-angle X-ray scattering (GIWAXS) was performed at the BioPACIFIC MIP user facilities at UC Santa Barbara. GIWAXS was used to evaluate the alignment of LCE films. Measurements were taken from homogeneously aligned (monodomain) nematic LCE films produced in the exact same way as described above, with the exception that the nematic director was uniform along the thickness of the film. Grazing incidence experiments enable scattering measurements through the surface of a thin films, for which similar transmission geometry experiments would be cumbersome. As the bottom half of the diffraction cone is absorbed by the substrate, only the upper half of the scattering pattern (Debye-Scherrer ring) is apparent (Supplementary Figure 1) [34]. The WAXS instrument was custom-built using a high brightness liquid metal jet X-ray source (Excillum MetalJet D2+ 70 keV) and a 4-megapixel hybrid photon-counting X-ray area detector (Dectris Eiger2 R 4M). WAXS data were collected using a 9.24 keV beam in 10-minute intervals at an incidence angle of approximately 1° at room temperature.

## Acknowledgements

This work was supported National Science Foundation under Award No. DMR-2041671 and Texas A&M University. This work was partially supported by the BioPACIFIC Materials Innovation Platform of the National Science Foundation under Award No. DMR-1933487.

## Conflict of Interest

The authors declare no conflict of interest.

## References

[1] X. Fan, X. Dong, A. C. Karacakol, H. Xie, M. Sitti, *Proceedings of the National Academy of Sciences* **2020**, *117*, 45 27916.

[2] X. Yang, R. Tan, H. Lu, T. Fukuda, Y. Shen, *Nature Communications* **2022**, *13*, 1 4156.

[3] E. Diller, N. Zhang, M. Sitti, *Journal of Micro-Bio Robotics* **2013**, *8*, 3 121.

[4] B. Saintyves, M. Spenko, H. M. Jaeger, *Science Robotics* **2024**, *9*, 86 eadh4130.

[5] W. Savoie, H. Tuazon, I. Tiwari, M. S. Bhamla, D. I. Goldman, *Soft Matter* **2023**, *19*, 10 1952.

[6] M. K. Abdelrahman, R. J. Wagner, M. S. Kalairaj, M. Zadan, M. H. Kim, L. K. Jang, S. Wang, M. Javed, A. Dana, K. A. Singh, et al., *Nature Materials* **2024**, 1–9.

[7] S. Ramaswamy, *Annu. Rev. Condens. Matter Phys.* **2010**, *1*, 1 323.

[8] F. Vernerey, E. Benet, L. Blue, A. Fajrial, S. L. Sridhar, J. Lum, G. Shakya, K. Song, A. Thomas, M. Borden, *Advances in colloid and interface science* **2019**, 263 38.

[9] R. P. Behringer, B. Chakraborty, *Reports on Progress in Physics* **2018**, *82*, 1 012601.

[10] R. J. Wagner, K. Such, E. Hobbs, F. J. Vernerey, *Journal of the Royal Society Interface* **2021**, *18*, 179 20210213.

[11] C. M. Grozinger, J. Richards, H. R. Mattila, *Apidologie* **2014**, 45 327.

[12] A. Worley, A. B. Sendova-Franks, N. R. Franks, *Royal Society Open Science* **2019**, *6*, 3 181626.

[13] V. P. Patil, H. Tuazon, E. Kaufman, T. Chakrabortty, D. Qin, J. Dunkel, M. S. Bhamla, *Science* **2023**, *380*, 6643 392.

[14] N. J. Mlot, C. A. Tovey, D. L. Hu, *Proceedings of the National Academy of Sciences* **2011**, *108*, 19 7669.

[15] C. Anderson, G. Theraulaz, J.-L. Deneubourg, *Insectes sociaux* **2002**, 49 99.

[16] M. Tennenbaum, Z. Liu, D. Hu, A. Fernandez-Nieves, *Nature materials* **2016**, *15*, 1 54.

[17] Y. Ozkan-Aydin, D. I. Goldman, M. S. Bhamla, *Proceedings of the National Academy of Sciences* **2021**, *118*, 6 e2010542118.

[18] P. C. Foster, N. J. Mlot, A. Lin, D. L. Hu, *Journal of Experimental Biology* **2014**, *217*, 12 2089.

[19] M. Tennenbaum, A. Fernandez-Nieves, *Physical Review E* **2017**, *96*, 5 052601.

[20] A. Deblais, S. Woutersen, D. Bonn, *Physical Review Letters* **2020**, *124*, 18 188002.

[21] J. Aguilar, T. Zhang, F. Qian, M. Kingsbury, B. McInroe, N. Mazouchova, C. Li, R. Maladen, C. Gong, M. Travers, et al., *Reports on Progress in Physics* **2016**, *79*, 11 110001.

[22] R. J. Wagner, F. J. Vernerey, *PLOS Computational Biology* **2022**, *18*, 2 e1009869.

[23] S. Li, B. Dutta, S. Cannon, J. J. Daymude, R. Avinery, E. Aydin, A. W. Richa, D. I. Goldman, D. Randall, *Science Advances* **2021**, *7*, 17 eabe8494.

[24] S. Li, R. Batra, D. Brown, H.-D. Chang, N. Ranganathan, C. Hoberman, D. Rus, H. Lipson, *Nature* **2019**, *567*, 7748 361.

[25] Y. Sawa, K. Urayama, T. Takigawa, V. Gimenez-Pinto, B. L. Mbanga, F. Ye, J. V. Selinger, R. L. Selinger, *Physical Review E—Statistical, Nonlinear, and Soft Matter Physics* **2013**, *88*, 2 022502.

[26] L. T. de Haan, A. P. Schenning, D. J. Broer, *Polymer* **2014**, *55*, 23 5885.

[27] M. Bergou, M. Wardetzky, S. Robinson, B. Audoly, E. Grinspan, In *ACM SIGGRAPH 2008 papers*, 1–12. **2008**.

[28] D. Tong, A. Choi, J. Joo, M. K. Jawed, *Extreme Mechanics Letters* **2023**, *58* 101924.

[29] E. Panagiotou, K. C. Millett, S. Lambropoulou, *Journal of Physics A: Mathematical and Theoretical* **2010**, *43*, 4 045208.

[30] A. W. Mahoney, N. D. Nelson, K. E. Peyer, B. J. Nelson, J. J. Abbott, *Applied Physics Letters* **2014**, *104*, 14.

[31] J. Boothby, T. Ware, *Soft Matter* **2017**, *13*, 24 4349.

[32] C. Perge, N. Taberlet, T. Gibaud, S. Manneville, *Journal of Rheology* **2014**, *58*, 5 1331.

[33] M. Dinkgreve, J. Paredes, M. M. Denn, D. Bonn, *Journal of non-Newtonian fluid mechanics* **2016**, *238* 233.

[34] A. Mahmood, J.-L. Wang, *Solar RRL* **2020**, *4*, 10 2000337.

## A Supplementary information

### A.1 List of supporting videos

#### Video S1: Entanglement and aggregation of ribbons.

Multi-angle view of aggregation of a ribbon dispersions with  $\theta = 10^\circ$  at  $65^\circ\text{C}$ .

#### Video S2: Response to the magnetic field.

The trajectories of the magnetic domain of a single  $\theta = 10^\circ$  ribbon under different temperatures are tracked in time. The video shows the tracked path (left panel), the actual motion of the ribbon (center panel), and the filtered path near 1.2 Hz (right panel) relating to the magnetic rotation.

#### Video S3: Aggregation experiment of different ribbon systems.

Comparison of representative aggregation experiments of: non-actuating ribbons (polydomain);  $\theta = [0, 10, 20]^\circ$  at  $65^\circ\text{C}$ ; and  $\theta = 10^\circ$  at  $T = [40, 65, 90, 120]^\circ\text{C}$ .

#### Video S4: Simulations of dynamic entanglement

Representative simulations of aggregation of 'sticky' and 'non-sticky' filaments with low ( $\theta = 10^\circ$  at  $65^\circ\text{C}$ ) and high ( $\theta = 10^\circ$  at  $90^\circ\text{C}$ ) curvatures.

#### Video S5: Aggregate response to cooling and heating.

Pre-formed aggregates ( $\theta = 10^\circ$  at  $65^\circ\text{C}$ ) are cooled to  $40^\circ\text{C}$  and heated to  $120^\circ\text{C}$ .

#### Video S6: Aggregate dissociation.

Pre-formed aggregates ( $\theta = 10^\circ$  at  $65^\circ\text{C}$ ) submerged in different viscosity oils are subjected to different field rotation speeds to induce dissociation.

### A.2 Supplementary data

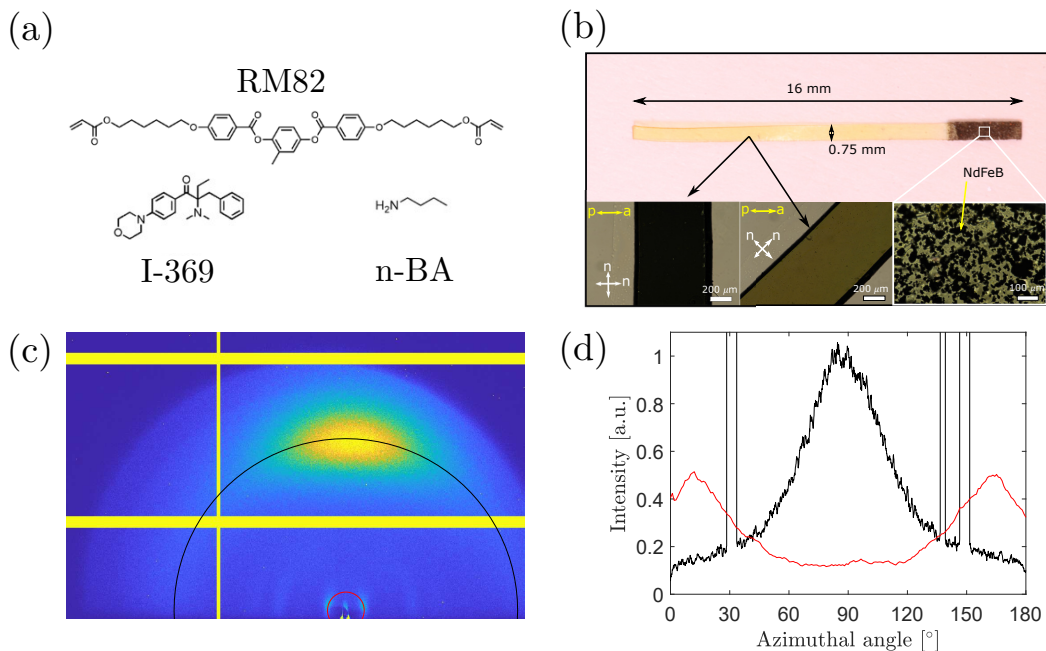


Figure S1: Overview of LCE chemistry, and ribbon composition. (a) Drawing of the molecular structure of the monomers (RM82, n-BA), and the photoinitiator (I-369) used to synthesize LCE. (b) Image of a single unactuated ribbon with polarized optical micrographs between parallel polarizers demonstrating birefringence indicative of a twisted nematic alignment, where 'p' and 'a' denote the polarizer and analyzer orientation, respectively, and 'n' denotes the orientation of the nematic director through the thickness of the film. (c) Diffractogram obtained using grazing-incidence wide-angle X-Ray scattering of a homogenously aligned (monodomain) surface-aligned LCE film indicating a well-aligned nematic. (d) Scattering intensity as a function of the azimuthal angle along the respectively colored rings in (c).

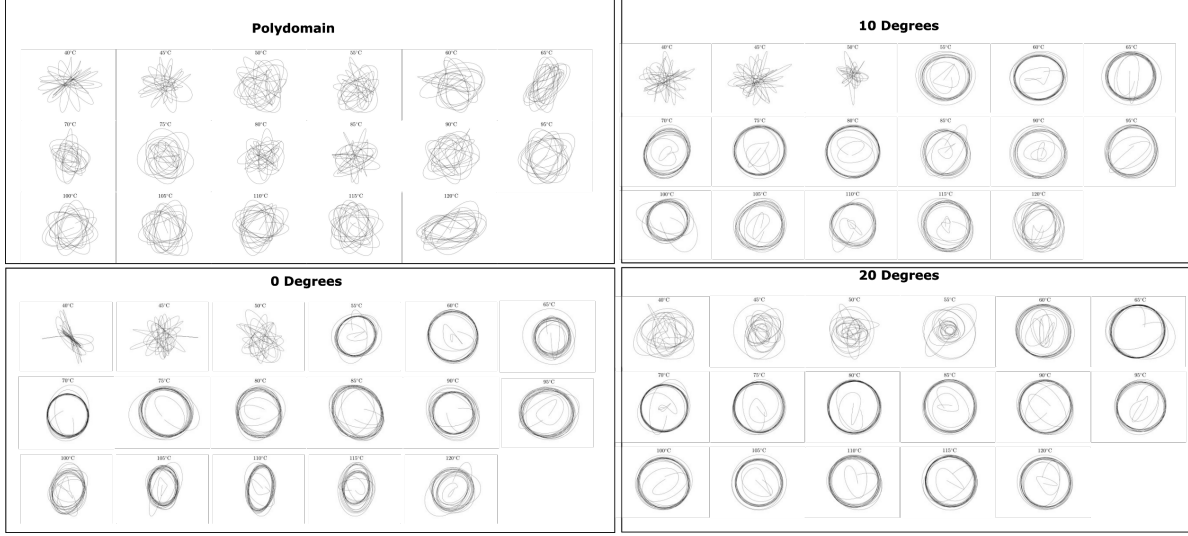


Figure S2: Magnetic domain trajectories sampled from different ribbon systems at different temperatures and filtered around 1.2 Hz.

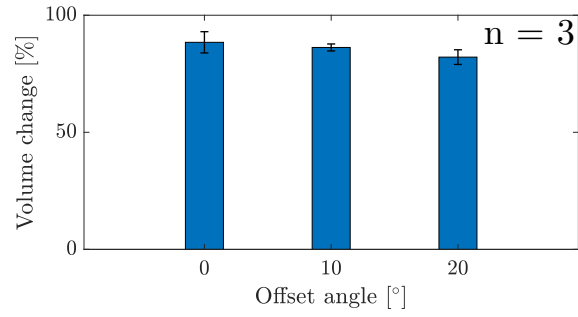


Figure S3: Change in absolute occupied volume between dispersed (1) and aggregated (3) states in Figure 1c for three different offset angles,  $\theta = [0, 10, 20]^\circ$ . Error bars represent the standard deviation,  $n = 3$ .

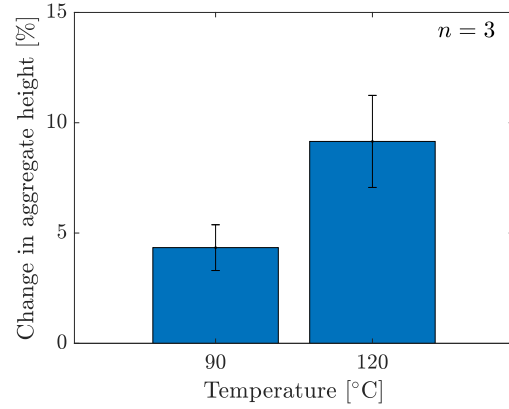


Figure S4: Average change and standard deviation in aggregate height, relative to the recorded value formed at  $65^\circ\text{C}$  for  $\theta = 10^\circ$  ribbons,  $n = 3$ .

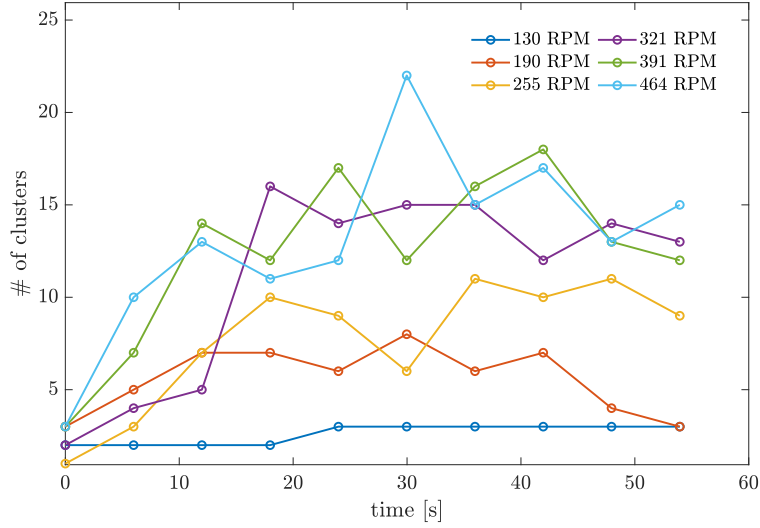


Figure S5: Example of raw data of the time evolution of the # of clusters in dissociation experiments at different field rotation speeds in the range [130,464] RPM, on a  $\theta = 10^\circ$  aggregate preformed at  $65^\circ\text{C}$  and 72 RPM.

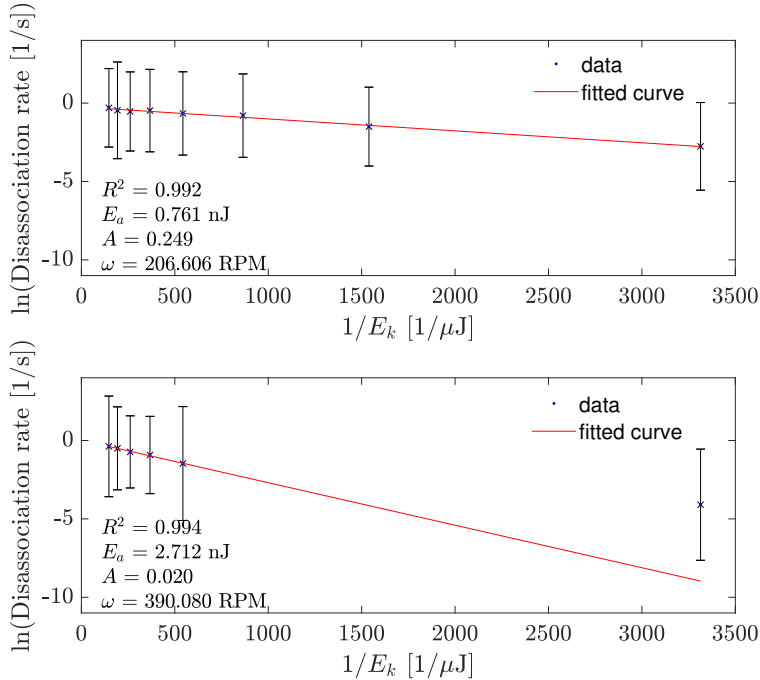


Figure S6: Linear regression of dissociation measurements to the proposed Arrhenius model for  $65^\circ\text{C}$  [top panel] and  $90^\circ\text{C}$  [bottom panel].

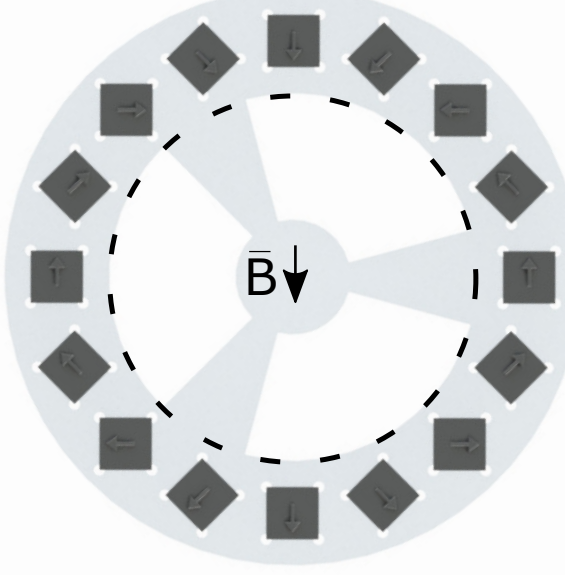


Figure S7: Schematic of a circular Halbach array (Halbach cylinder,  $k = 2$ ) housing 16 block magnets arranged in a circle. The dashed line represent the area in which the magnetic field is uniform.

### A.3 Mathematical model

We formulate a simplified mathematical model for the ribbon aggregation process by treating each ribbon as a rigid body subject to forces and torques. In particular, our model includes the effect of an external driving torque, arising from the magnetic field, a random force accounting for the drift of each ribbon, and contact forces and torques arising from their many-body interactions. The simulations shown in Figure 4 are performed by discretizing the ribbons, and then calculating the forces and torques on each ribbon in the discretized framework. Below we describe these forces and torques in more detail.

Treated as a rigid body, the state of a single ribbon can be constructed by rotating a translating a representative ribbon. Specifically, let  $\gamma(s) \in \mathbb{R}^3$  for  $s \in [0, L]$  be the centerline of the ribbon, where  $s$  is an arc length parameter in  $L$  is the length of the ribbon. Suppose further that the curve  $\gamma$  is centered at the origin, so  $\int \gamma ds = 0$ . The  $i$ 'th ribbon at time  $t$ ,  $\gamma_i(s, t)$  can then be described in terms of a  $3 \times 3$  rotation matrix  $Q_i$  and a translation  $\mathbf{R}_i$

$$\gamma_i(s, t) = Q_i(t)\gamma(s) + \mathbf{R}_i(t) = \mathbf{r}_i(t, s) + \mathbf{R}_i(t)$$

Setting  $\mathbf{r}_i(s, t) = Q_i(t)\gamma(s)$ , the ribbon velocity decomposes into rotational and translations parts

$$\dot{\gamma}_i = \boldsymbol{\omega}_i \times \mathbf{r}_i + \dot{\mathbf{R}}_i \quad (1)$$

where the angular velocity  $\boldsymbol{\omega}$  can be written in index notation using the Levi-Civita symbol  $\epsilon_{abc}$  as  $\epsilon_{abc}\omega_a = \dot{Q}_{bd}Q_{cd}$ . The angular velocity therefore satisfies

$$\dot{\mathbf{r}}_i = \dot{Q}_i\gamma = \dot{Q}_i Q_i^\top Q_i\gamma = \boldsymbol{\omega}_i \times \mathbf{r}_i$$

A state of the  $N$ -ribbon system can be given in terms of  $N$  rotations and translations

$$\{Q_1, \mathbf{R}_1, Q_2, \mathbf{R}_2, \dots, Q_N, \mathbf{R}_N\} \quad (2)$$

An allowed  $N$ -ribbon configuration must also have the property that no two ribbons intersect each other. To capture contact, we approximate each ribbon as a tube with circular cross-sections of radius  $h$  and with centerline  $\gamma_i(s, t)$ . Using the approximation, an allowed configuration must satisfy the constraint

$$|\gamma_i(s) - \gamma_j(s')| \geq 2h \quad \forall i, j, s, s' \quad (3)$$

Additionally, the ribbons are in a domain  $\Omega \subset \mathbb{R}^3$ . This constraint can be written

$$\gamma_i(s) \in \Omega, \quad d(\gamma_i(s), \partial\Omega) > h \quad \forall i, s \quad (4)$$

Each ribbon is subject to an external driving torque  $\tau^{\text{ext}}$ , an external stochastic drift force  $\mathbf{F}^{\text{ext}}$ , as well as contact forces and torques arising from other ribbons  $\mathbf{F}^{\text{con}}$ ,  $\tau^{\text{con}}$  and from the boundary  $\mathbf{F}^{\text{bdry}}$ ,  $\tau^{\text{bdry}}$ . We treat the dynamics as overdamped and neglect hydrodynamics, obtaining the following simplified equations of motion

$$\eta_T \dot{\mathbf{x}}_i = \mathbf{F}_i^{\text{ext}} + \mathbf{F}_i^{\text{con}} + \mathbf{F}_i^{\text{bdry}} \quad (5a)$$

$$\eta_R \dot{\boldsymbol{\omega}}_i = \boldsymbol{\tau}_i^{\text{ext}} + \boldsymbol{\tau}_i^{\text{con}} + \boldsymbol{\tau}_i^{\text{bdry}} \quad (5b)$$

Although this framework corresponds to a simple diagonal resistance matrix, it is sufficient to capture the aggregation dynamics of the ribbons. The external forces and torque do not depend on the state of the ribbon aggregate, and therefore have relatively simple expressions. In particular, we take the external torque to be constant with magnitude  $b$

$$\boldsymbol{\tau}_i^{\text{ext}} = b \mathbf{e}_z \quad (6)$$

The external force is stochastic, given by

$$\mathbf{F}_i^{\text{ext}} = \cos \theta_i \mathbf{e}_x + \sin \theta_i \mathbf{e}_y + \sqrt{2D_x} \xi_i^z \mathbf{e}_z \quad (7a)$$

$$\dot{\theta}_i = \sqrt{2D_\theta} \xi_i^\theta \quad (7b)$$

where  $\xi_i^z, \xi_i^\theta$  are independent white noise processes satisfying

$$\langle \xi_i^z(t) \xi_j^z(t') \rangle = \delta_{ij} \delta(t - t') \quad \langle \xi_i^\theta(t) \xi_j^\theta(t') \rangle = \delta_{ij} \delta(t - t')$$

The fact that the  $z$ -direction is treated differently from the  $x, y$ -directions reflects the fact that the experiments typically take place in domains with horizontal extent much larger than vertical extent.

The expressions for contact forces and torques require a more careful accounting of the positions and overlaps of all the ribbons. There are several approaches for formulating these interactions [13, 27]. Here we construct contact forces by approximating each ribbon as a tube with circular cross-sections of radius  $h$  (equation 3). We can quantify the contact between the  $i$ 'th and  $j$ 'th ribbons by setting  $\mathbf{d}_{ij}(s, \sigma) = \gamma_i(s) - \gamma_j(\sigma)$  and  $\hat{\mathbf{d}}_{ij} = \mathbf{d}_{ij}/|\mathbf{d}_{ij}|$ , and defining  $p_{ij}$  as follows

$$p_{ij}(s, \sigma) = 1 - \frac{\mathbf{d}_{ij}(s, \sigma)}{2h_{\text{eff}}}$$

where  $h_{\text{eff}} - h$  is small. If  $h_{\text{eff}} = h$ , then  $p_{ij} = 0$  when  $\gamma_i(s), \gamma_j(\sigma)$  are touching and  $p = 1$  when  $\gamma_i(s), \gamma_j(\sigma)$  overlap completely. Choosing  $h_{\text{eff}} \neq h$  has the desirable effect of smoothing out the contact region and the associated contact forces [28]. From  $p$  we can construct a potential energy  $V(p)$  for soft contacts

$$V(p) = \frac{K}{2} p^2 + K p_0 \left( \frac{1}{4} p^4 + \frac{1}{6} p^6 + \frac{1}{8} p^8 \right) \quad \text{for } p > 0$$

$$V(p) = 0 \quad \text{for } p < 0$$

where the parameter  $K$  sets the magnitude of the repulsive contact forces and  $p_0$  is a constant that sets the rate at which the potential stiffens. In addition, we assume that ribbons which are in contact must overcome an energy barrier in order to separate. This can be thought of as a ‘sticky’ adhesion force. A ribbon-ribbon contact which is on the point of separating has  $p_{ij}(s, \sigma) = 0$  and  $\dot{p}_{ij} < 0$ . The additional adhesion term can therefore be taken to be proportional to  $\delta(p_{ij})\Theta(-\dot{p}_{ij})\hat{\mathbf{d}}_{ij}$  where  $\Theta$  is the Heaviside step function. Including adhesion effects, the contact force density on the  $i$ 'th ribbon due the  $j$ 'th ribbon is then

$$\mathbf{f}_{ij}^{\text{con}}(s) = - \int_0^L d\sigma \left( \frac{dV}{dp} \Big|_{p_{ij}(s, \sigma)} - \alpha \delta(p_{ij}(s, \sigma)) \Theta(-\dot{p}_{ij}(s, \sigma)) \right) \hat{\mathbf{d}}_{ij}(s, \sigma)$$

where  $\alpha$  determines adhesion strength. From this expression we can write down the total contact force and torque on the  $i$  ribbon

$$\mathbf{F}_i^{\text{con}} = \sum_j \int_0^L ds \mathbf{f}_{ij}^{\text{con}}(s) \quad (8a)$$

$$\boldsymbol{\tau}_i^{\text{con}} = \sum_j \int_0^L ds \mathbf{r}_i(s) \times \mathbf{f}_{ij}^{\text{con}}(s) \quad (8b)$$

Finally boundary forces act to keep each ribbon confined to a domain  $\Omega$ . The boundary forces act at  $\gamma_i(s)$  if  $d(\gamma_i(s), \partial\Omega) \leq h$  or equivalent if  $\Theta(h - d(\gamma_i(s), \partial\Omega)) = 1$ . To write down the boundary force, for  $\mathbf{x} \in \Omega$ , let

$P(\mathbf{x}) \in \partial\Omega$  be the closest point to  $\mathbf{x}$  on the boundary of  $\Omega$ . Additionally, for  $\mathbf{y} \in \partial\Omega$ , let  $\mathbf{n}(\mathbf{y})$  be the inward normal to  $\partial\Omega$  at  $\mathbf{y}$ . Then the boundary force density on the  $i$ 'th ribbon is

$$\mathbf{f}_i^{\text{bdry}}(s) = K_b \Theta(h - d(\gamma_i(s), \partial\Omega)) \mathbf{n}(P(\gamma_i(s)))$$

where  $K_b$  sets the strength of the boundary force. The boundary forces and torques are then

$$\mathbf{F}_i^{\text{bdry}} = \int_0^L ds \mathbf{f}_i^{\text{bdry}}(s) \quad (9a)$$

$$\boldsymbol{\tau}_i^{\text{bdry}} = \int_0^L ds \mathbf{r}_i(s) \times \mathbf{f}_i^{\text{bdry}}(s) \quad (9b)$$

Our mathematical model for ribbon aggregation is given by equations (5)-(9).

### A.3.1 Geometry and topology of ribbon aggregates

Geometric and topological quantities can be used to understand the structure of the ribbon aggregates formed by the model described above. For example the contact structure of these aggregates follows from constructing the contact graph, where each ribbon is a vertex and two vertices are joined by an edge if the corresponding ribbons are touching. More precisely, let  $A_{ij}$  be 1 if ribbons  $i$  and  $j$  are touching, and 0 otherwise.  $A_{ij}$  is therefore an adjacency matrix for the ribbon contact graph. The number of connected components of this graph provides a measure of aggregation of the ribbons.

The topological connectivity of ribbon aggregates can be quantified using the open linking number

$$Lk_{ij}^O = \frac{1}{4\pi} \int ds d\sigma \frac{(\gamma_i(s) - \gamma_j(\sigma)) \cdot (\gamma'_i(s) \times \gamma'_j(\sigma))}{|\gamma_i(s) - \gamma_j(\sigma)|^3} \quad (10)$$

For closed curves, the above integral yields a topological invariant whose value remains constant as the curves are deformed and moved, provided they do not pass through each other. For open curves, such as the ribbons we study here, this integral varies continuously as the open curves move. However, the open linking number nonetheless provides important information about how intertwined two curves are [13, 29]. Furthermore, the open linking numbers also allow us to measure the total amount of linking between the  $i$ 'th ribbon and the rest of the aggregate

$$T_i^{Lk}(\gamma_1, \dots, \gamma_N) = \sum_j |Lk_{ij}^O|$$

The average value of this parameter is the linking per filament,  $T^{Lk}$ , which gives a measure of the overall total intertwining within an aggregate [13]

$$T^{Lk}(\gamma_1, \dots, \gamma_N) = \langle T_i^{Lk} \rangle = \frac{1}{N} \sum_{i,j} |Lk_{ij}^O|$$

A random choice of  $N$  ribbons within a domain  $\Omega$  will typically have small, nonzero linking per filament  $T^{Lk}$ . This non-zero ‘background linking’ can be quantified finding the average value of  $T^{Lk}$  for random collections of  $N$  ribbons. Let  $(\tilde{\gamma}_1, \dots, \tilde{\gamma}_N)$  be  $N$  ribbons chosen uniformly at random in a domain  $\Omega$ , subject to the contact and boundary constraints described above (equation 3). The excess linking per filament can then be defined as

$$T_{ex}^{Lk}(\gamma_1, \dots, \gamma_N) = T^{Lk}(\gamma_1, \dots, \gamma_N) - \langle T^{Lk}(\tilde{\gamma}_1, \dots, \tilde{\gamma}_N) \rangle \quad (11)$$

To avoid distortions due to the background linking, in Figure 4, we show the excess linking per filament.

#### A.4 Activation energy

The activation energy,  $E_a$ , represents the minimal amount of rotational kinetic energy,  $E_k$ , required to dissociate the physical bonds in the cluster. To estimate it, we employ the Arrhenius-like model

$$k = Ae^{-\frac{E_a}{E_k}},$$

where  $k$  [1/s] is the dissociation rate (measured number of steady state clusters per 20 s) and  $A$  [1/s] is a constant that can be considered as the rate of collisions in the system (since in our system the rotational kinetic energy is the driving force for all types of lateral motions and subsequently collisions). We can approximate the rotational kinetic energy,  $E = 1/2I\omega^2$ , of a mildly coiled ribbon using the moment of inertia for a hoop rotating about its cylindrical axis,  $I = MR^2$ , where  $M \approx 0.5 \times 10^{-6} kg$  is the ribbon mass,  $R$  is its radius, and  $\omega$  is the magnetic field rotation speed. Using the formula for a circle with perimeter  $l = 2\pi R$ , the radius of the ribbon with  $l = 16$  mm can be estimated as approximately 2.5 mm (consistent with the curvature measurements in section 2.1). The linear regression (Figure 6) is then fitted to the Arrhenius plot for 65°C yields the activation energy value  $E_a \approx 0.761$  nJ (95% CI: [0.694, 0.827] nJ), and  $A \approx 0.78$  1/s. Since the critical activation energy required for a ribbon to induce dissociation also takes the form of a rotational kinetic energy,  $E_a = 1/2I\omega_c^2$ , we can substitute the fitted and previously calculated values to obtain  $\omega_c \approx 206.6$  RPM (95% CI: [197.3, 215.5] RPM), as heuristically estimated above. Similarly, the results for 90°C yield  $E_a \approx 2.712$  nJ (95% CI: [2.327, 3.096] nJ) and  $A \approx 0.9798$  1/s, corresponding to  $\omega_c \approx 390.1$  RPM (95% CI: [361.4, 416.8] RPM).